Available online at www.sciencedirect.com
ScienceDirect
Journal of Solid State Chemistry 179 (2006) 3357–3364
JOURNAL OF SOLID STATE CHEMISTRY
www.elsevier.com/locate/jssc

Local environments and dynamics of hydrogen atoms in protonated forms of ion-exchangeable layered perovskites estimated by solid-state ^{1}H NMR

Shinsuke Tani[a], Yoshihiko Komori[b], Shigenobu Hayashi[b], Yoshiyuki Sugahara[a,*]

[a]*Department of Applied Chemistry, School of Science and Engineering, Waseda University, Shinjuku-ku, Tokyo 169-8555, Japan*
[b]*Research Institute of Instrumentation Frontier, National Institute of Advanced Industrial Science and Technology (AIST), Tsukuba Central 5, 1-1-1 Higashi, Tsukuba, Ibaraki 305-8565, Japan*

Received 13 April 2006; received in revised form 21 June 2006; accepted 21 June 2006
Available online 11 July 2006

Abstract

The local environments and dynamics of hydrogen atoms in five samples of protonated forms of ion-exchangeable layered perovskites, Dion–Jacobson-type $H[LaNb_2O_7]$ and $H[LaTa_2O_7]$, Ruddlesden–Popper-type $H_2[SrTa_2O_7]$ and $H_2[La_2Ti_3O_{10}]$, and $H_{1.8}[(Sr_{0.8}Bi_{0.2})Ta_2O_7]$ derived from an Aurivillius phase, $Bi_2Sr_2Ta_2O_9$, have been investigated by solid-state ^{1}H nuclear magnetic resonance spectroscopy (NMR). Solid-state ^{1}H NMR with a magic-angle spinning technique conducted at room temperature reveals that the mean electron densities around the ^{1}H nuclei in these protonated forms are relatively low, and that they decrease in the following order: $H_{1.8}[(Sr_{0.8}Bi_{0.2})Ta_2O_7] > H[LaNb_2O_7] > H_2[SrTa_2O_7] > H[LaTa_2O_7] > H_2[La_2Ti_3O_{10}]$. The temperature-dependent solid-state ^{1}H broad-line NMR spectra measured at 140–400 K reveal a decrease in the signal width for all of these five samples upon heating due to motional narrowing. The NMR spectra of $H[LaNb_2O_7]$ and $H[LaTa_2O_7]$ are different from the other three protonated forms due to the weaker dipole–dipole interactions at low temperatures and lower mobility of the hydrogen atoms at high temperatures.
© 2006 Elsevier Inc. All rights reserved.

Keywords: Solid-state ^{1}H NMR; Motional narrowing; Magic-angle spinning; Variable-temperature measurement; Layered perovskite; Protonated form

1. Introduction

Layered compounds possessing perovskite-like slabs are referred to as "layered perovskites." Layered perovskites consisting of negatively charged (100)-terminated perovskite-like slabs ($[A_{n-1}B_nO_{3n+1}]$) and interlayer cations (M) are called ion-exchangeable layered perovskites (Fig. 1) and are classified into two families: the Ruddlesden–Popper phases, $M_2[A_{n-1}B_nO_{3n+1}]$ [1,2], and the Dion–Jacobson phases, $M[A_{n-1}B_nO_{3n+1}]$ [3,4] (where A = Sr, Ca, etc.; B = Nb, Ta, Ti, etc.; M = Li, Na, K, etc.; and n is the number of the corner sharing BO_6 octahedron in a perovskite-like slab along the stacking direction). Acid treatment of these ion-exchangeable layered perovskites leads to the formation of their protonated forms, $H_2[A_{n-1}B_nO_{3n+1}]$ and $H[A_{n-1}B_nO_{3n+1}]$ [5,6]. The conversion of several Aurivillius phases ($Bi_2A_{n-1}B_nO_{3n+3}$), another homologous series of layered perovskites with (100)-terminated perovskite-like slabs [7–9] into protonated forms of ion-exchangeable layered perovskites has recently been reported [10–17]. Compositions expected from the structures proposed for the starting Aurivillius phases, $Bi_2O_2[A_{n-1}B_nO_{3n+1}]$, are Ruddlesden–Popper-type, $H_2[A_{n-1}B_nO_{3n+1}]$, but the actual amounts of hydrogen atoms are slightly lower, typically 1.8 per $[A_{n-1}B_nO_{3n+1}]$, because of the presence of cation disorders occurring between the trivalent bismuth cations and divalent A-site cations in the Aurivillius phases ($(A,Bi)_2O_2[(A,Bi)_{n-1}B_nO_{3n+1}]$).

Protonated forms of ion-exchangeable layered perovskites exhibit interesting properties, including acidity [18,19], proton conductivity [20,21], and photocatalytic activity [16,22,23]. These properties should be related to the

*Corresponding author. Fax: +81 3 5286 3204.
E-mail address: ys6546@waseda.jp (Y. Sugahara).

0022-4596/$ - see front matter © 2006 Elsevier Inc. All rights reserved.
doi:10.1016/j.jssc.2006.06.030

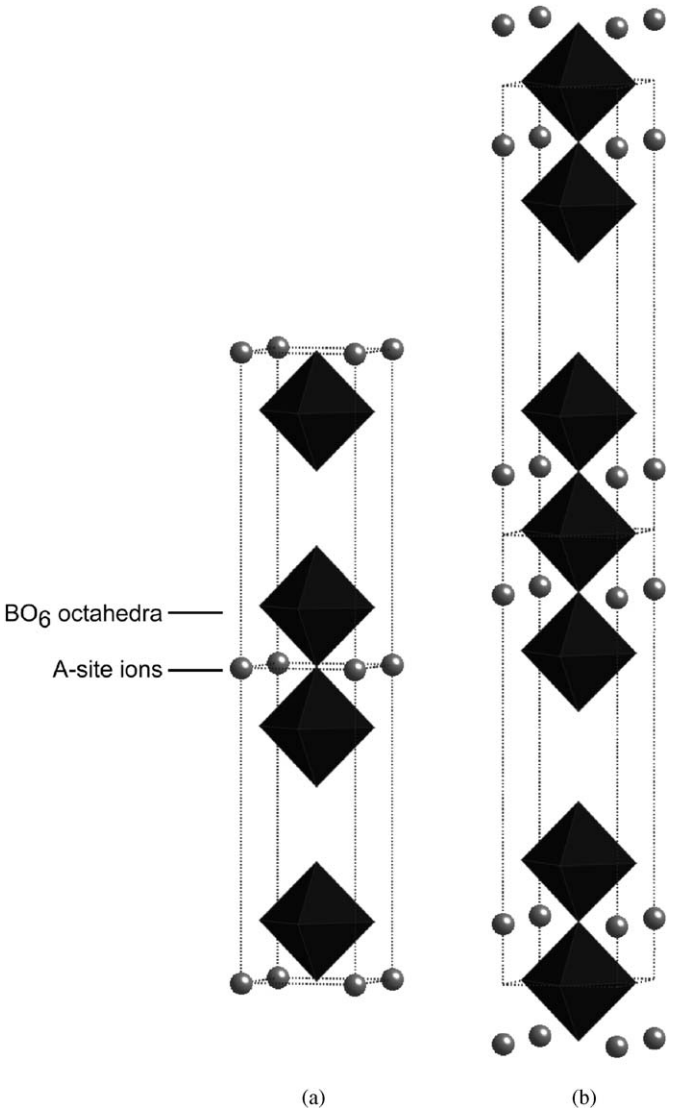

Fig. 1. Ideal structures of protonated forms of ion-exchangeable layered perovskites: (a) $H_x[AB_2O_7]$ ($n = 2$); and (b) $H_x[A_2B_3O_{10}]$ ($n = 3$).

local environments and dynamics of hydrogen atoms in the interlayer space. To date, however, investigations of the local environments and dynamics of the hydrogen atoms have been limited. Solid-state ^{1}H nuclear magnetic resonance (NMR) is a powerful technique for analyzing local structures near hydrogen atoms, such as the characteristics of chemical bonds and dynamics of hydrogen atoms in solids, and the dynamics of hydrogen atoms have often been discussed based on temperature- and frequency-dependencies of relaxation times and/or line shapes. Solid-state ^{1}H NMR has been applied extensively to investigations of brønsted acidities of hydrogen atoms [24–27]. Thus, besides Raman spectroscopy [28] and the intercalation behavior of bases [29], solid-state ^{1}H NMR has been employed to evaluate the local environments of the hydrogen atoms in protonated forms of ion-exchangeable layered perovskites [21,30–32]. Mangamma et al. [30] investigated the dynamics of hydrogen atoms in $H[La_2NbTi_2O_{10}]\cdot 1.5H_2O$ by line shape analysis of variable-temperature study and relaxation time measurements, and discussed a mechanism for the dynamics of hydrogen atoms. Tambelli et al. [21] reported the temperature dependence of the line shape and spin–lattice relaxation time, T_1, of $H[Pb_2Nb_3O_{10}]\cdot nH_2O$, and the proposed conduction mechanism was consistent with a two-dimensional structure. Takagaki et al. [19] recently reported on the local environments of hydrogen atoms in $H[Sr_2Nb_3O_{10}]$ and its nano-sheets (perovskite-like slabs) derived through exfoliation by solid-state ^{1}H NMR with magic-angle spinning (MAS). To the best of our knowledge, however, there has so far been no detailed study of factors affecting the chemical shifts and dynamics of hydrogen atoms for protonated forms of various ion-exchangeable layered perovskites.

We report here a solid-state ^{1}H NMR study of five samples of protonated forms of ion-exchangeable layered perovskites: Dion–Jacobson-type $H[LaNb_2O_7]$ and $H[LaTa_2O_7]$, Ruddlesden–Popper-type $H_2[SrTa_2O_7]$ and $H_2[La_2Ti_3O_{10}]$, and $H_{1.8}[(Sr_{0.8}Bi_{0.2})Ta_2O_7]$ derived from an Aurivillius phase, $Bi_2SrTa_2O_9$. $H[LaNb_2O_7]$, $H[LaTa_2O_7]$, $H_2[SrTa_2O_7]$, and $H_{1.8}[(Sr_{0.8}Bi_{0.2})Ta_2O_7]$ possess double-layered structures, while the structure of $H_2[La_2Ti_3O_{10}]$ is triple-layered. Besides the results of the ^{1}H MAS NMR study, we present temperature-dependent broad-line NMR spectra to explore the dynamics of hydrogen atoms. The focus is placed on motional narrowing behavior in the variable temperature study.

2. Experimental section

2.1. Instrumentation

The compositions of starting ion-exchangeable layered perovskites and the Aurivillius phase, as well as the protonated forms derived, were determined by inductively-coupled plasma emission spectrometry (ICP; Threrm0 Jarrell Ash, IRIS/AP) or X-ray fluorescence spectroscopy (XRF; Rigaku, RIX2100). The X-ray diffraction (XRD) patterns were recorded on a Rigaku RINT-2500 diffractometer (monochromated Cu $K\alpha$ radiation). Rietveld analysis was performed using the RIETAN program [33]. Solid-state ^{1}H MAS NMR spectra were measured on a JEOL JNM-CMX400 spectrometer with the ordinary single-pulse sequence and a spinning rate of 8 kHz. Chemical shifts in the ^{1}H MAS NMR spectra were reported with respect to external tetramethylsilane. Before the ^{1}H MAS NMR measurements, the samples were dried at 120 °C for 1 day. Solid-state ^{1}H broad-line NMR spectra were measured on a Bruker ASX200 spectrometer using the solid echo pulse sequence [34]. The samples for the ^{1}H broad–line NMR were dried at 120 °C in vacuo and sealed in an NMR tube in vacuo.

2.2. Preparation of $H[LaNb_2O_7]$ from $RbLaNb_2O$

$RbLaNb_2O_7$ was prepared as described in the previous report [18]. The XRD pattern of $RbLaNb_2O_7$ can be indexed on the basis of a tetragonal cell ($a = 0.38886(5)$, $c = 1.0984(1)$ nm, space group: $P4/mmm$). $RbLaNb_2O_7$ was treated with 6 M HNO_3 at 60 °C for 72 h. After acid treatment, the product was centrifuged, washed with water, and dried at 120 °C. The conversion of $RbLaNb_2O_7$ into $H[LaNb_2O_7]$ by acid treatment was confirmed by ICP. The lattice parameters (tetragonal cell: $a = 0.38913(8)$, $c = 1.0470(2)$ nm) of $H[LaNb_2O_7]$ are consistent with those shown in the previous report ($a = 0.3894(3)$, $c = 1.0459(7)$ nm) [18].

2.3. Preparation of $H[LaTa_2O_7]$ from $RbLaTa_2O_7$

The preparation of $RbLaTa_2O_7$ was conducted based on the method described in the previous report [35]. The XRD pattern of $RbLaTa_2O_7$ can be indexed on the basis of a tetragonal cell ($a = 0.3885(2)$, $c = 1.1106(6)$ nm). $RbLaTa_2O_7$ was dispersed in 6 M HNO_3 at 60 °C for 168 h. After acid treatment, the product was centrifuged, washed with water, and dried at 120 °C. The conversion of $RbLaTa_2O_7$ into $H[LaTa_2O_7]$ by acid treatment was confirmed by XRF. The XRD patterns of $H[LaTa_2O_7]$ can be indexed on the basis of a tetragonal cell ($a = 0.3880(2)$, $c = 1.066(1)$ nm).

2.4. Preparation of $H_2[SrTa_2O_7]$ from $Li_2SrTa_2O_7$

$Li_2SrTa_2O_7$ was prepared by a solid-state reaction, which is slightly modified from the reported procedure [36]; a stoichiometric mixture of Li_2CO_3, $SrCO_3$ and Ta_2O_5 was heated at 600 °C for 12 h, 1100 °C for 6 h and 1100 °C for 6 h with intermittent grinding. The XRD pattern of $Li_2SrTa_2O_7$ can be indexed on the basis of a tetragonal cell ($a = 0.39476(9)$ nm, $c = 1.8185(4)$ nm) [37]. Acid treatment of $Li_2SrTa_2O_7$ was performed as described in the previous report [38]. After acid treatment, the crude product was centrifuged, washed with water, and dried at 120 °C. The complete leaching of lithium was confirmed by ICP. The XRD pattern of $H_2[SrTa_2O_7]$ is consistent with that reported previously [38].

2.5. Preparation of $H_2[La_2Ti_3O_{10}]$ from $K_2La_2Ti_3O_{10}$

$K_2La_2Ti_3O_{10}$ was prepared by a solid-state reaction. A mixture of K_2CO_3, La_2O_3, and TiO_2 [1.25:1:1 (in molar ratio)] was heated at 1100 °C for 72 h with intermittent grinding every 24 h. After calcinations, the product was washed with water and air-dried. The XRD pattern of $K_2La_2Ti_3O_{10}$ can be indexed on the basis of a tetragonal cell ($a = 0.3853(2)$, $c = 2.978(2)$ nm) [6]. $K_2La_2Ti_3O_{10}$ was dispersed in 1 M HNO_3 at ambient temperature for 72 h. After acid treatment, the product was centrifuged, washed with water, and dried at 120 °C. ICP demonstrated the conversion of $K_2La_2Ti_3O_{10}$ into $H_2[La_2Ti_3O_{10}]$. The XRD patterns of $H_2[La_2Ti_3O_{10}]$ can be indexed on the basis of a tetragonal cell ($a = 0.38114(7)$, $c = 2.7478(8)$ nm), whose lattice parameters are consistent with those presented in the previous report ($a = 0.3820(9)$, $c = 2.766(7)$ nm) [6].

2.6. Preparation of $H_{1.8}[(Sr_{0.8}Bi_{0.2})Ta_2O_7]$ from $Bi_2SrTa_2O_9$

The preparation of $Bi_2SrTa_2O_9$ was conducted based on the method described in the previous report [11]. The XRD pattern of $Bi_2SrTa_2O_9$ can be indexed on the basis of an orthorhombic cell ($a = 0.5520(1)$ nm, $b = 0.5519(1)$ nm, $c = 2.5051(5)$ nm). Acid treatment of $Bi_2SrTa_2O_9$ was performed as described in the previous report [11]. After acid treatment, the product was centrifuged, washed with water, and dried at 120 °C. The conversion of $Bi_2SrTa_2O_9$ into $H_{1.8}[(Sr_{0.8}Bi_{0.2})Ta_2O_7]$ by acid treatment was confirmed by ICP. The XRD pattern of $H_{1.8}[(Sr_{0.8}Bi_{0.2})Ta_2O_7]$ can be indexed on the basis of a tetragonal cell ($a = 0.3897(5)$, $c = 0.978(2)$ nm), and its lattice parameters are consistent with the previously reported values ($a = 0.391(4)$, $c = 0.98(1)$ nm).

3. Results and discussion

3.1. Structural characterization

Fig. 2 shows the XRD patterns of the protonated forms. Except for $H[LaTa_2O_7]$ and $H_2[SrTa_2O_7]$, their detailed structural characterization has been reported. Since the XRD patterns of both $H[LaNb_2O_7]$ and $H[LaTa_2O_7]$ can be indexed with a tetragonal cell possessing very similar lattice parameters ($H[LaNb_2O_7]$, $a = 0.38913(8)$, $c = 1.0470(2)$ nm; $H[LaTa_2O_7]$, $a = 0.3880(2)$, $c = 1.066(1)$ nm), the structure of $H[LaTa_2O_7]$ seems to be identical to that of $H[LaNb_2O_7]$.

Two types of stacking sequence are generally observed in protonated forms of layered perovskites: a *P*-type stacking sequence without displacement and an *I*-type stacking sequence with displacement in both the *a* and *b* directions, $(a+b)/2$ (Fig. 3) [11]. If the (100) reflection (in the tetragonal cell with $a \approx b \approx 0.39$ nm) is present in the XRD pattern, the stacking sequence is considered to be of the *P*-type. Thus, the stacking sequences of both $H[LaTa_2O_7]$ and $H[LaNb_2O_7]$ are classified into the *P*-type, and it is proposed that the stacking sequence of $H_2[La_2Ti_3O_{10}]$ is of the *I*-type [6].

The XRD patterns of $H_2[SrTa_2O_7]$ and $H_{1.8}[(Sr_{0.8}Bi_{0.2})Ta_2O_7]$ are similar to each other, results consistent with their structural and compositional similarity; both of these compounds are double-layered tantalates, and the differences between these two compounds are the compositions of the *A*-sites [$Sr \leftrightarrow (Sr_{0.8}Bi_{0.2})$] and the resulting hydrogen contents ($2.0 \leftrightarrow 1.8$) per $[ATa_2O_7]$. While the XRD pattern of $H_{1.8}[(Sr_{0.8}Bi_{0.2})Ta_2O_7]$ can be indexed on the basis of a tetragonal cell ($a = 0.3897(5)$, $c = 0.978(2)$ nm), the XRD

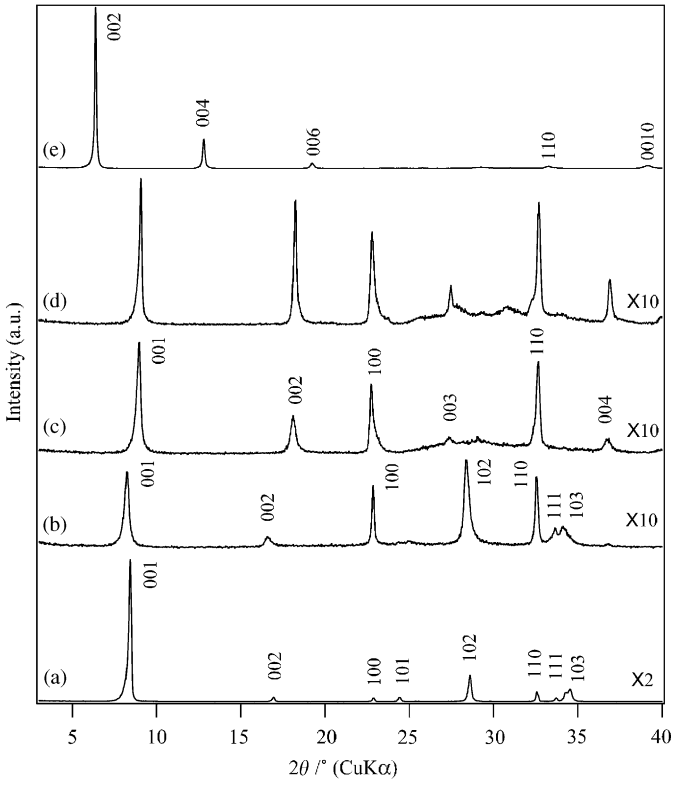

Fig. 2. XRD patterns of protonated forms of ion-exchangeable layered perovskites: (a) $H[LaNb_2O_7]$; (b) $H[LaTa_2O_7]$; (c) $H_{1.8}[(Sr_{0.8}Bi_{0.2})Ta_2O_7]$; (d) $H_2[SrTa_2O_7]$; and (e) $H_2[La_2Ti_3O_{10}]$.

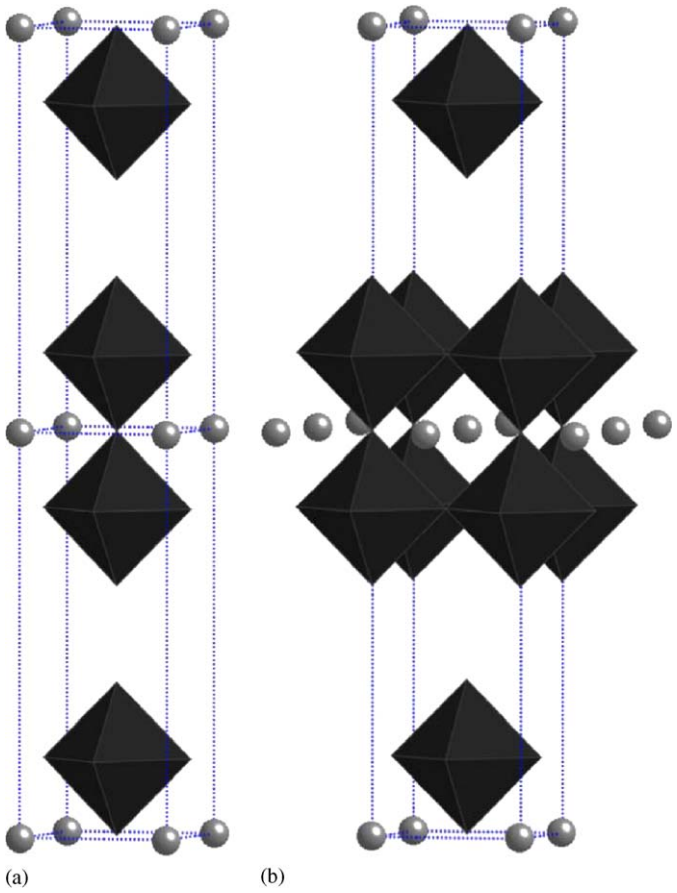

Fig. 3. Stacking sequences in protonated forms of ion-exchangeable layered perovskites: (a) *P*-type; and (b) *I*-type.

pattern of $H_2[SrTa_2O_7]$ cannot be indexed, a finding consistent with the previous report.

3.2. Solid-state ^1H MAS NMR

Fig. 4 demonstrates the ^1H MAS NMR spectra of the examined protonated forms. In the spectrum of $H[LaNb_2O_7]$, a sharp signal is observed at 10.5 ppm. The spectrum of $H[LaTa_2O_7]$ exhibits a signal at 12.9 ppm with a shoulder signal at 7.7 ppm. $H_{1.8}[(Sr_{0.8}Bi_{0.2})Ta_2O_7]$ shows a broad signal at 9.4 ppm. The spectrum of $H_2[SrTa_2O_7]$ consists of a signal at 9.4 ppm and an additional broad shoulder signal at 12.1 ppm. The spectrum of $H_2[La_2Ti_3O_{10}]$ consists of a relatively broad signal at 14.0 ppm. The line width reflects the ordered arrangement of the hydrogen bonds, because it originates from chemical shift dispersion.

The ^1H chemical shift depends on the electron density: the presence of a signal at a lower frequency (in an upfield region) reflects a larger shielding effect caused by the high electron density around the ^1H nuclei. For hydroxy-containing compounds such as hydrous metal oxides and metal hydroxides, in particular, chemical shifts are mainly subjected to brønsted acidity (a tendency to become H^+) and hydrogen bond formation [24,39]. In terms of the effect of hydrogen bonds, the hydrogen atoms in the hydroxy groups in a layered silicate, RUB-18 is involved in very strong hydrogen bonds to exhibit a signal at 15.9 ppm [40] while the hydrogen atoms in the hydroxy groups in kaolinite, in which weak hydrogen bonds are present, exhibit a signal at 2.8 ppm [41]. When no hydrogen bond is present, on the other hand, chemical shifts are subjected to brønsted acidities; a larger chemical shift indicates stronger acidity [25–27]. The hydrogen atoms of the hydroxy groups in zeolite HY, for example, which possesses brønsted-type acidic hydrogen, exhibit signals at 4.2–8.0 ppm, and the hydroxy groups exhibiting large chemical shifts (6.8–8.0 ppm) show the significant catalytic activity [42]. In the present study, the main signals are observed at around 8–14 ppm and are similar to or larger than the chemical shifts of hydrogen atoms in zeolite HY, indicating that the electron densities around the ^1H nuclei in these protonated forms are relatively low.

In order to compare the electron densities around the ^1H nuclei in these five protonated forms, we calculated the mean chemical shifts of the hydrogen atoms on the basis of integrals, since some of the spectra are composed of multiple signals. Thus, the estimated mean electron densities decrease in the following order: $H_{1.8}[(Sr_{0.8}Bi_{0.2})Ta_2O_7]$ (10.4 ppm) > $H[LaNb_2O_7]$ (10.6 ppm) > $H_2[SrTa_2O_7]$ (11.8 ppm) > $H[LaTa_2O_7]$ (11.9 ppm) > $H_2[La_2Ti_3O_{10}]$ (13.4 ppm). Both acidic character and

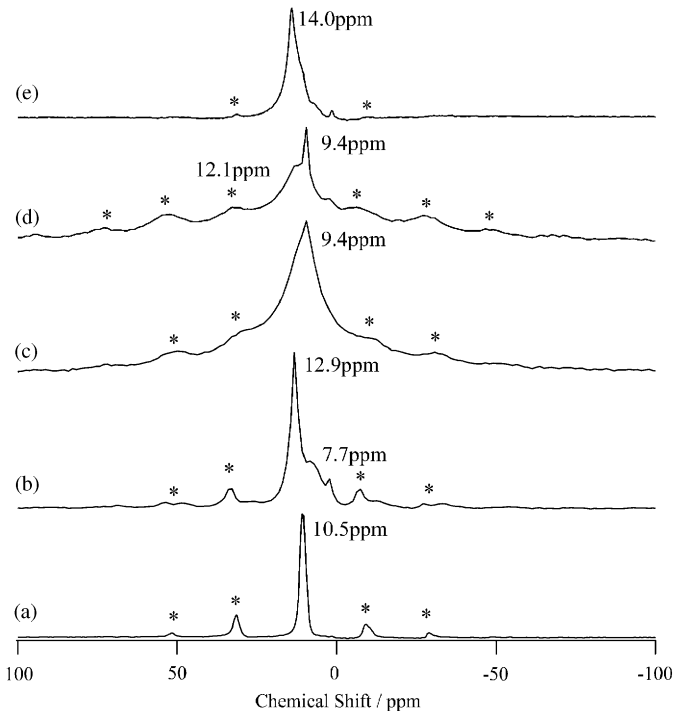

Fig. 4. Solid-state ^{1}H MAS NMR spectra of protonated forms of ion-exchangeable layered perovskites: (a) $H[LaNb_2O_7]$; (b) $H[LaTa_2O_7]$; (c) $H_{1.8}[(Sr_{0.8}Bi_{0.2})Ta_2O_7]$; (d) $H_2[SrTa_2O_7]$; and (e) $H_2[La_2Ti_3O_{10}]$. The spinning side bands are marked with asterisks.

hydrogen bond formation with oxygen atoms on an adjacent layer can contribute to low electron density. The intercalation behavior of $H_{1.8}[(Sr_{0.8}Bi_{0.2})Ta_2O_7]$ through acid–base reactions indicates that the hydrogen atoms are only weakly acidic [29]. In addition, the hydrogen atoms of anhydrous isolated nano-sheets of $H[Sr_2Nb_3O_{10}]$ showed a signal at 1.6 ppm, while the hydrogen atoms of anhydrous stacked $H[Sr_2Nb_3O_{10}]$, where strong hydrogen bonds were formed, exhibited a signal at 10.0 ppm [19]. Thus, hydrogen bond formation appears to contribute significantly to low electron density.

The chemical shift of $H[LaTa_2O_7]$ (main signal, 12.9 ppm; average value, 11.9 ppm) is larger than that of $H[LaNb_2O_7]$ (main signal, 10.5 ppm; average value, 10.6 ppm). Since the structures of $H[LaNb_2O_7]$ and $H[LaTa_2O_7]$ appear to be identical to each other, their chemical shifts reflect the differences in electron densities caused by *B*-site ions, Nb^{5+} and Ta^{5+}. Abe et al. [43] have investigated the ion-exchange properties of niobium oxide hydrate and tantalum oxide hydrate . They have reported that the acidity of amorphous tantalum oxides is higher than that of niobium. Thus, similar differences in brønsted acidity could be expected for $H[LaTa_2O_7]$ and $H[LaNb_2O_7]$, leading to the variation in chemical shifts.

3.3. Hydrogen dynamics

Fig. 5 shows the temperature dependence of solid-state ^{1}H broad-line NMR spectra of the protonated forms to study the dynamics of interlayer hydrogen atoms. In solid-state ^{1}H broad-line NMR spectra, signals are broadened mainly by a dipole–dipole interaction among hydrogen atoms. The dipole–dipole interaction is averaged out when the mobility of the hydrogen atoms becomes sufficiently high. The signal width decreases, therefore, as the mobility of hydrogen tends to increase. When the mobility of hydrogen reaches a specific region, in particular, a drastic decrease in the signal width, the so-called 'motional narrowing', occurs [34]. The change of the signal width in the other regions, on the contrary, is not significant.

In the spectra of all the protonated forms, the signals measured at 400 K are sharper than the corresponding spectra measured at 140 K. It is known that the second moment, $\delta\omega^2$, can be expressed by the following[44]:

$$\delta\omega^2 = \delta\omega''^2_0 + \delta\omega'^2_0 \frac{2}{\pi} \tan^{-1}[\delta\omega\tau_c], \quad (1)$$

where $\delta\omega^2$, second moment at temperature T; $\delta\omega''^2_0$, second moment after narrowing; $\delta\omega'^2_0$, difference between the second moments before and after narrowing; τ_c, correlation time. The correlation time τ_c can be derived as follows:

$$\tau_c = \tau_0 \exp\left(\frac{E_a}{RT}\right), \quad (2)$$

where E_a, activation energy; τ_0, correlation time at infinite temperature; R, gas constant; and T, absolute temperature.

Second moment analysis (Fig. 6) clearly indicates that motional narrowing regions are present in the temperature range from 140 to 400 K. The temperature dependence of the second moment is fitted to Eq. (1), as shown in Fig. 6. We assume that there is no distribution in the motional rate in order to obtain approximate mean values, although the NMR line shapes indicate the presence of distribution. The results of second moment analysis clearly indicate that translational diffusion of hydrogen atoms occurs at high temperature in the interlayer space of these protonated forms. Whereas motional narrowing is essentially completed below 400 K for $H_{1.8}[(Sr_{0.8}Bi_{0.2})Ta_2O_7]$, $H_2[SrTa_2O_7]$ and $H_2[La_2Ti_3O_{10}]$, 400 K is not sufficient for complete motional narrowing for $H[LaNb_2O_7]$ and $H[LaTa_2O_7]$. E_a and τ_0 are estimated from the Arrhenius plots (Fig. 7) as follows: $H_2[SrTa_2O_7]$, $E_a = 7.4$ kJ/mol, $\tau_0 = 5.6 \times 10^{-7}$ s; $H_2[La_2Ti_3O_{10}]$, $E_a = 9.3$ kJ/mol, $\tau_0 = 2.4 \times 10^{-7}$ s; $H_{1.8}[(Sr_{0.8}Bi_{0.2})Ta_2O_7]$, $E_a = 22$ kJ/mol, $\tau_0 = 4.6 \times 10^{-9}$ s; $H[LaTa_2O_7]$, $E_a = 5.6$ kJ/mol, $\tau_0 = 3.3 \times 10^{-6}$ s; $H[LaNb_2O_7]$, $E_a = 17$ kJ/mol, $\tau_0 = 2.7 \times 10^{-7}$ s. Since the phase transition was reported at 389 K for $H_2SrTa_2O_7$ [38], we could not exclude the presence of phase transitions induced by hydrogen dynamics in this temperature range. The observed variation in the second moment, however, provides no indication of phase transition in the measurement temperature range (the effect of the phase transition at 389 K on second moment variation is unclear, since 389 K is very close to the highest temperature, 400 K).

When the spectra measured at 140 K, which is below the motional narrowing region, are compared, the signal

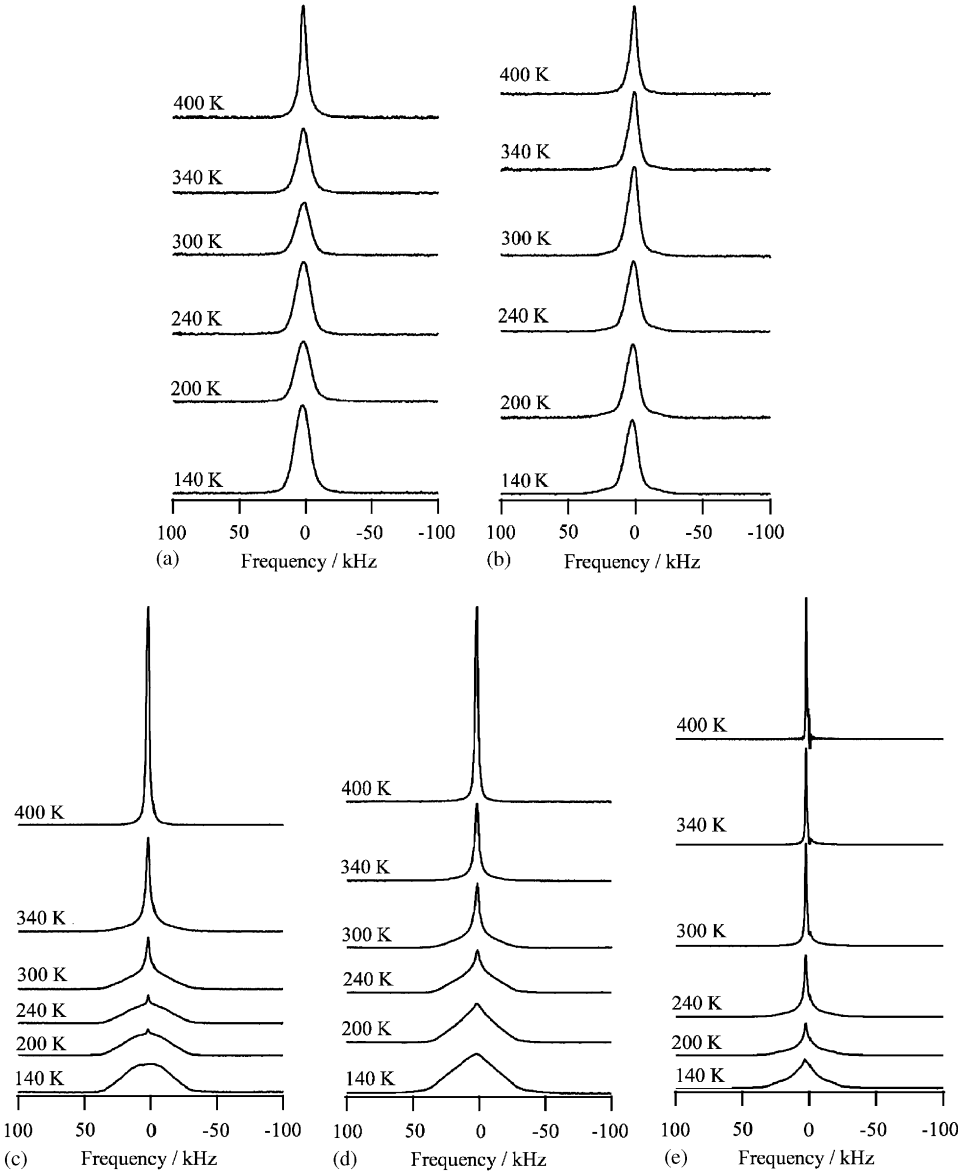

Fig. 5. Variable-temperature solid-state ^{1}H NMR spectra of protonated forms of ion-exchangeable layered perovskites: (a) $H[LaNb_2O_7]$; (b) $H[LaTa_2O_7]$; (c) $H_{1.8}[(Sr_{0.8}Bi_{0.2})Ta_2O_7]$; (d) $H_2[SrTa_2O_7]$; and (e) $H_2[La_2Ti_3O_{10}]$.

widths in the spectra of $H[LaTa_2O_7]$ and $H[LaNb_2O_7]$ are narrower than those in the spectra of $H_2[La_2Ti_3O_{10}]$, $H_{1.8}[(Sr_{0.8}Bi_{0.2})Ta_2O_7]$, and $H_2[SrTa_2O_7]$. The hydrogen atom mobilities are not expected to influence the line shapes significantly at 140 K. Thus, the dipole–dipole interaction is governed by the hydrogen–hydrogen distances; the shorter hydrogen–hydrogen distances lead to stronger dipole–dipole interaction among hydrogen atoms to increase the signal widths.

The interlayer surface geometries of these protonated forms are essentially identical with each other, indicating that the hydrogen atom distance in the interlayer space can be directly related to both the number of hydrogen atoms per perovskite unit $[A_{n-1}B_nO_{3n+1}]$ and the type of stacking sequence, irrespective of n [13]. In Dion–Jascobson phases, $H[A_{n-1}B_nO_{3n+1}]$, the number of hydrogen atoms corresponds to half the number of apical oxygen atoms located on the interlayer surface. Since two apical oxygen atoms in adjacent slabs face each other in the *P*-type stacking sequence, the hydrogen atoms are expected to be located near two facing apical oxygen atoms, resulting in a hydrogen atom distance close to the a parameter (~0.39 nm). In the Ruddlesden–Popper phases, $H_2[A_{n-1}B_nO_{3n+1}]$, on the other hand, the number of hydrogen atoms is equal to that of the apical oxygen atoms located on the interlayer surface. In the *I*-type stacking sequence, the distance separating apical oxygen atoms along the *ab* plane should be $a/\sqrt{2}$, ~0.28 nm. Since it is reasonable to assume that all the hydrogen atoms are located near the apical oxygen atoms, the distance is expected to be close to 0.28 nm (the exact value depends on the relative positions of two hydrogen atoms along the

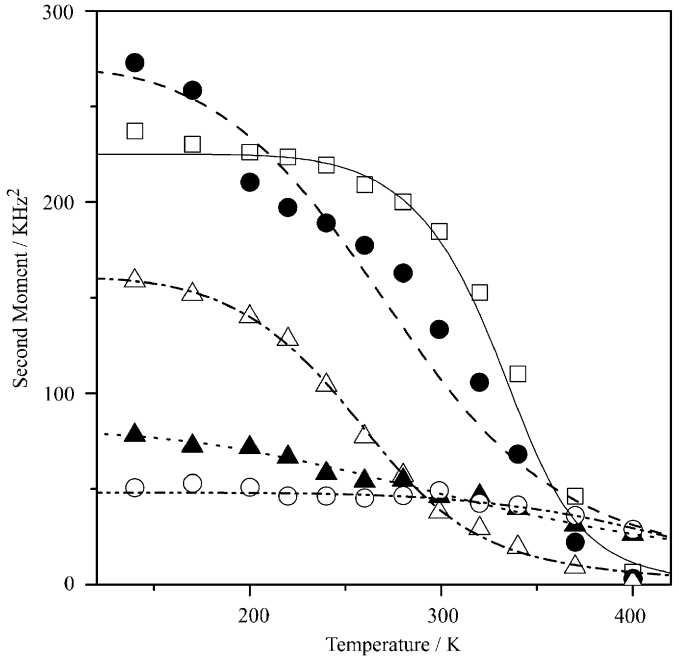

Fig. 6. Second moment versus temperature: ○, $H[LaNb_2O_7]$; ▲, $H[LaTa_2O_7]$; □, $H_{1.8}[(Sr_{0.8}Bi_{0.2})Ta_2O_7]$; ●, $H_2[SrTa_2O_7]$; and △: $H_2[La_2Ti_3O_{10}]$.

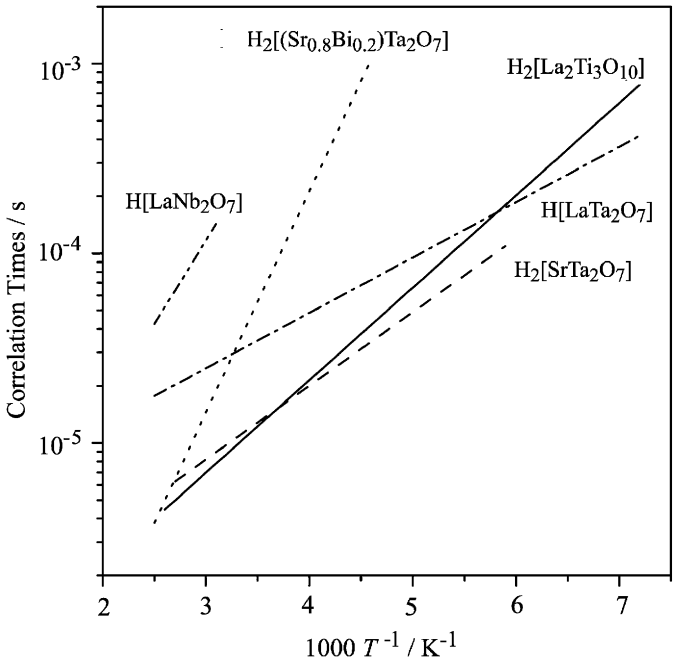

Fig. 7. Correlation times (τ_c) calculated from date plotted in Fig. 6.

c-axis and the precise positions of the hydrogen atoms with respect to the apical oxygen atoms). Thus, the hydrogen–hydrogen distances in Dion–Jascobson-type $H[LaTa_2O_7]$ and $H[LaNb_2O_7]$ are much longer than those of Ruddlesden–Popper-type $H_2[La_2Ti_3O_{10}]$.

The environments of the hydrogen atoms in $H_{1.8}[(Sr_{0.8}Bi_{0.2})Ta_2O_7]$ and $H_2[SrTa_2O_7]$ are much more complicated. In $H_{1.8}[(Sr_{0.8}Bi_{0.2})Ta_2O_7]$, both *P*-type and *I*-type stacking sequences are present [11], and the amount of hydrogen per perovskite unit $[A_{n-1}B_nO_{3n+1}]$ should be slightly lower that that in the Ruddlesden–Popper phases. In the *I*-type stacking sequence, the hydrogen–hydrogen distances are nearly equal to or larger than that in the Ruddlesden–Popper phases, ~0.28 nm. In the *P*-type stacking sequence, on the contrary, a pair of hydrogen atoms is expected to be present near two apical oxygen atoms that are facing each other at least partially, leading to the presence of two hydrogen atoms with very short distances. In terms of the hydrogen atoms in $H_2[SrTa_2O_7]$, whose structure is not completely clarified [38], no detailed structural consideration is possible. Based on the high hydrogen content (as a Ruddlesden–Popper phase, 2.0 per $[A_{n-1}B_nO_{3n+1}]$), the hydrogen–hydrogen distances in the interlayer space seem to be much shorter than that in Dion–Jascobson-type $H[LaTa_2O_7]$ and $H[LaNb_2O_7]$.

Among the spectra measured at 400 K, on the contrary, the signal widths in the spectra of $H[LaTa_2O_7]$ and $H[LaNb_2O_7]$ are wider than those in the spectra of $H_2[La_2Ti_3O_{10}]$, $H_{1.8}[(Sr_{0.8}Bi_{0.2})Ta_2O_7]$, and $H_2[SrTa_2O_7]$. As suggested by the second moment analysis in Fig. 6, 400 K is insufficient for $H[LaTa_2O_7]$ and $H[LaNb_2O_7]$ to cause complete motional narrowing, while motional narrowing is essentially completed at 400 K for $H_2[La_2Ti_3O_{10}]$, $H_{1.8}[(Sr_{0.8}Bi_{0.2})Ta_2O_7]$, and $H_2[SrTa_2O_7]$. These observations suggest that the mobility of the interlayer hydrogen atoms of $H[LaTa_2O_7]$ and $H[LaNb_2O_7]$ is lower than that of $H_2[La_2Ti_3O_{10}]$, $H_{1.8}[(Sr_{0.8}Bi_{0.2})Ta_2O_7]$, and $H_2[SrTa_2O_7]$ at 400 K.

Both $H[LaTa_2O_7]$ and $H[LaNb_2O_7]$ possess the *P*-type stacking sequence, in which two apical oxygen atoms in adjacent slabs face each other. The other three protonated forms, by contrast, either do not possess the *P*-type stacking sequence or possess the *P*-type stacking sequence only partially. It is therefore reasonable to assume that hydrogen mobility in the *P*-type stacking sequence up to 400 K is limited. The narrowing behavior of $H_2[La_2Ti_3O_{10}]$ is very different from that of $H[LaNb_2O_7]$ and $H[LaTa_2O_7]$; the signal becomes very sharp in the spectrum measured at 400 K. Thus, the hydrogen atoms in $H_2[La_2Ti_3O_{10}]$ seem to be more mobile than those in $H[LaNb_2O_7]$ and $H[LaTa_2O_7]$ at higher temperatures. In a similar fashion, the hydrogen atoms in $H_{1.8}[(Sr_{0.8}Bi_{0.2})Ta_2O_7]$ and $H_2[SrTa_2O_7]$ are also mobile at higher temperatures. It should be noted that stacking disorders are present in $H_{1.8}[(Sr_{0.8}Bi_{0.2})Ta_2O_7]$ [11] and $H_2[SrTa_2O_7]$ [38]. In $H_{1.8}[(Sr_{0.8}Bi_{0.2})Ta_2O_7]$, moreover, the layer charge per $[(Sr_{0.8}Bi_{0.2})Ta_2O_7]$ is −1.8, not −2 as in the Ruddlesden–Popper phases, indicating that the number of protons near apical oxygen are probably not uniform. These disorders seem to increase the mobility of hydrogen atoms in $H_{1.8}[(Sr_{0.8}Bi_{0.2})Ta_2O_7]$ and $H_2[SrTa_2O_7]$. It should also be noted that spectra below 300 K consist of a broad part and a sharp part for four protonated phases ($H[LaTa_2O_7]$, $H_{1.8}[(Sr_{0.8}Bi_{0.2})Ta_2O_7]$, $H_2[SrTa_2O_7]$, and $H_2[La_2Ti_3O_{10}]$). The sharp part is considered to undergo motional narrowing, while the mobility of the hydrogen atoms exhibiting the broad part is insufficient for complete motional narrowing.

4. Conclusions

We have demonstrated that the local environments and dynamics of hydrogen atoms in five protonated forms of layered perovskites, $H[LaNb_2O_7]$, $H[LaTa_2O_7]$, $H_2[SrTa_2O_7]$, $H_{1.8}[(Sr_{0.8}Bi_{0.2})Ta_2O_7]$, and $H_2[La_2Ti_3O_{10}]$, can be estimated by solid-state ^1H NMR. The chemical shifts of ^1H MAS NMR reflect electron densities around the ^1H nuclei of hydrogen atoms, and the electron densities estimated from the mean chemical shifts decrease in the following order: $H_{1.8}[(Sr_{0.8}Bi_{0.2})Ta_2O_7] > H[LaNb_2O_7] > H_2[SrTa_2O_7] > H[LaTa_2O_7] > H_2[La_2Ti_3O_{10}]$. The ^1H broad-line NMR spectra indicate the occurrence of motional narrowing in the temperature range (140–400 K) for all of these five samples of protonated forms, indicating the presence of translational diffusion of hydrogen atoms in the interlayer space. Among the spectra measured at 140 K, the signal widths in the spectra of Dion–Jacobson-type $H[LaNb_2O_7]$ and $H[LaTa_2O_7]$ are much narrower than those in the spectra of $H_{1.8}[(Sr_{0.8}Bi_{0.2})Ta_2O_7]$, $H_2[SrTa_2O_7]$ and $H_2[La_2Ti_3O_{10}]$. Since hydrogen mobilities do not appear to affect the signal width significantly at this temperature, the narrower signal widths in the Dion–Jacobson phases are ascribable to weaker dipole–dipole interactions due to much longer hydrogen–hydrogen distances. Among the spectra measured at 400 K, on the contrary, the signal widths in the spectra of $H[LaNb_2O_7]$ and $H[LaTa_2O_7]$ are wider, results reflecting the lower mobilities of their hydrogen atoms. The present results clearly demonstrate that the local environments and dynamics of the hydrogen atoms in protonated forms of ion-exchangeable layered perovskites depend on the hydrogen density in the interlayer space as well as the stacking sequence of the perovskite-like slabs $[A_{n-1}B_nO_{3n+1}]$.

Acknowledgments

The authors thank Prof. Kazuyuki Kuroda of the Waseda University Department of Applied Chemistry for his valuable discussions. This work was financially supported by the Grant-in-Aid for Scientific Research (No. 14350462) from the Ministry of Education, Science, Sports, and Culture, Japan and by 21COE "Practical Nano-Chemistry" from MEXT, Japan.

References

[1] S.N. Ruddlesden, P. Popper, Acta Crystallogr. 10 (1957) 538–539.
[2] S.N. Ruddlesden, P. Popper, Acta Crystallogr. 11 (1958) 54–55.
[3] M. Dion, M. Ganne, M. Tournoux, Mater. Res. Bull. 16 (1981) 1429–1435.
[4] A.J. Jacobson, J.W. Johnson, J.T. Lewandowski, Inorg. Chem. 24 (1985) 3727–3729.
[5] A.J. Jacobson, J.T. Lewandowski, J.W. Johnson, J. Less-Common Met. 116 (1986) 137–146.
[6] J. Gopalakrishnan, V. Bhat, Inorg. Chem. 26 (1987) 4299–4301.
[7] B. Aurivillius, Ark. Kemi 1 (1949) 463–480.
[8] B. Aurivillius, Ark. Kemi 1 (1949) 499–512.
[9] B. Aurivillius, Ark. Kemi 2 (1950) 519–527.
[10] W. Sugimoto, M. Shirata, Y. Sugahara, K. Kuroda, J. Am. Chem. Soc. 121 (1999) 11601–11602.
[11] Y. Tsunoda, M. Shirata, W. Sugimoto, Z. Liu, O. Terasaki, K. Kuroda, Y. Sugahara, Inorg. Chem. 40 (2001) 5768–5771.
[12] W. Sugimoto, M. Shirata, K. Kuroda, Y. Sugahara, Chem. Mater. 14 (2002) 2946–2952.
[13] R.E. Schaak, T.E. Mallouk, Chem. Mater. 14 (2002) 1455–1471.
[14] R.E. Schaak, T.E. Mallouk, Chem. Commun. (2002) 706–707.
[15] M. Kudo, H. Ohkawa, W. Sugimoto, N. Kumada, Z. Liu, O. Terasaki, Y. Sugahara, Inorg. Chem. 42 (2003) 4479–4484.
[16] M. Kudo, S. Tsuzuki, K. Katsumata, A. Yasumori, Y. Sugahara, Chem. Phys. Lett. 393 (2004) 12–16.
[17] S. Tahara, Y. Sugahara, Recent Dev. Inorg. Chem. 4 (2004) 13–34.
[18] J. Gopalakrishnan, V. Bhat, B. Raveau, Mater. Res. Bull. 22 (1987) 413–417.
[19] A. Takagaki, M. Sugisawa, D. Lu, J.N. Kondo, M. Hara, K. Domen, S. Hayashi, J. Am. Chem. Soc. 125 (2003) 5479–5485.
[20] K. Toda, Y. Kameo, S. Kurita, M. Sato, J. Alloys Compds. 234 (1996) 19–25.
[21] C.E. Tambelli, J.P. Donoso, C.J. Magon, A.C.D. Ângelo, A.O. Florentino, M.J. Saeki, Solid State Ionics 136–137 (2000) 243–247.
[22] K. Domen, J.N. Kondo, M. Hara, T. Takata, Bull. Chem. Soc. Japan 73 (2000) 1307–1331.
[23] A. Kudo, J. Ceram. Soc. Japan 109 (2001) S81–S88.
[24] D. Freude, M. Hunger, H. Pfeifer, W. Schwieger, Chem. Phys. Lett. 128 (1986) 62–66.
[25] D. Freude, M. Hunger, H. Pfeifer, Z. Phys. Chem. 152 (1987) 171–182.
[26] H. Pfeifer, J. Chem. Soc. Faraday Trans. 1 84 (1988) 3777–3783.
[27] E. Brunner, H.G. Karge, H. Pfeifer, Z. Phys. Chem. 176 (1992) 173–183.
[28] S.-H. Byeon, S.-O. Lee, H. Kim, J. Solid State Chem. 130 (1997) 110–116.
[29] Y. Tsunoda, W. Sugimoto, Y. Sugahara, Chem. Mater. 15 (2003) 632–635.
[30] G. Mangamma, V. Bhat, J. Gopalakrishnan, S.V. Bhat, Solid State Ionics 58 (1992) 303–309.
[31] G. Okada, S. Ohmiya, S. Matsushima, K. Kobayashi, Denki Kagaku 60 (1992) 336–338.
[32] S. Nishimoto, M. Matsuda, M. Miyake, J. Solid State Chem. 178 (2005) 811–818.
[33] F. Izumi, in: R.A. Young (Ed.), Rietveld Analysis, Oxford University Press, Oxford, 1993, pp. 236–253.
[34] C.P. Slichter, Principles of Magnetic Resonance, Springer, Berlin, 1990.
[35] K. Toda, M. Sato, J. Mater. Chem. 6 (1996) 1067–1071.
[36] N. Floros, C. Michel, M. Hervieu, B. Raveau, J. Mater. Chem. 9 (1999) 3101–3106.
[37] N.S.P. Bhuvanesh, M.P. Crosnier-Lopez, H. Duroy, J.-L. Fourquet, J. Mater. Chem. 9 (1999) 3093–3100.
[38] N.S.P. Bhuvanesh, M.-P. Crosnier-Lopez, H. Duroy, J.-L. Fourquet, J. Mater. Chem. 10 (2000) 1685–1692.
[39] C.I. Ratcliffe, J.A. Ripmeester, J.S. Tse, Chem. Phys. Lett. 120 (1985) 427–432.
[40] I. Wolf, H. Gies, C.A. Fyfe, J. Phys. Chem. B 103 (1999) 5933–5938.
[41] S. Hayashi, T. Ueda, K. Hayamizu, E. Akiba, J. Phys. Chem. 96 (1992) 10928–10933.
[42] D. Freude, T. Fröhlich, M. Hunger, H. Pfeifer, G. Scheler, Chem. Phys. Lett. 98 (1983) 263–266.
[43] M. Abe, T. Kotani, S. Awano, in: P.A. Williams, A. Dyer (Eds.), Advances in Ion Exchange for Industry and Research, Springer, Berlin, 1999, pp. 199–211.
[44] A. Abragam, The Principles of Nuclear Magnetic Resonance, Clarendon Press, Oxford, 1961.